

Lifetimes of excited states in ^{16}C as a benchmark for ab initio developments

M. Mathy¹, M. Petri^{2,a}, R. Roth¹, L. Wagner¹, S. Heil¹,
A. D. Ayangeakaa^{3,10}, S. Bottoni^{3,11}, M. P. Carpenter³, H. L. Crawford⁴,
P. Fallon⁴, J. Elson⁵, J. Kinnison⁵, T. Lauritsen³, I.-Y. Lee⁴,
A. O. Macchiavelli⁶, S. Paschalidis², W. Revol³, D. G. Sarantites⁵,
I. Syndikus¹, S. Tabor⁷, M. Wiedeking^{8,9}, S. Zhu³

¹Institut für Kernphysik, Technische Universität Darmstadt, Darmstadt, Germany

²School of Physics, Engineering and Technology, University of York, Heslington, York, UK

³Physics Division, Argonne National Laboratory, Argonne, Illinois, USA

⁴Nuclear Science Division, Lawrence Berkeley National Laboratory, Berkeley, USA

⁵Chemistry Department, Washington University, St. Louis, Missouri, USA

⁶Physics Division, Oak Ridge National Laboratory, Oak Ridge, Tennessee, USA

⁷Department of Physics, Florida State University, Tallahassee, Florida, USA

⁸SSC Laboratory, iThemba LABS, PO Box 722, Somerset West, South Africa

⁹School of Physics, University of the Witwatersrand, Johannesburg, South Africa

¹⁰Present Address: Department of Physics and Astronomy, University of North Carolina at Chapel Hill, Chapel Hill, North Carolina 27599, USA and Triangle Universities Nuclear Laboratory, Duke University, Durham, North Carolina 27708, USA

¹¹Present Address: Dipartimento di Fisica, Università degli Studi di Milano and INFN Sez. Milano, Milano, Italy

Received: date / Accepted: date

Abstract Lifetimes of higher-lying states (2_2^+ and 4_1^+) in ^{16}C have been measured, employing the Gammasphere and Microball detector arrays, as key observables to test and refine ab initio calculations based on interactions developed within chiral Effective Field Theory. The presented experimental constraints to these lifetimes of $\tau(2_2^+) = [244, 446]$ fs and $\tau(4_1^+) = [1.8, 4]$ ps, combined with previous results on the lifetime of the 2_1^+ state of ^{16}C , provide a rather complete set of key observables to benchmark the theoretical developments. We present No-Core Shell-Model calculations using state-of-the-art chiral 2- (NN) and 3-nucleon (3N) interactions at next-to-next-to-next-to-leading order for both the NN and the 3N contributions and a generalized natural-orbital basis (instead of the conventional harmonic oscillator single-particle basis) which reproduce, for the first time, the experimental findings remarkably well. The level of agreement of the new calculations as compared to the CD-Bonn meson-exchange NN interaction is notable and presents a critical benchmark for theory.

Keywords lifetimes · transition strengths · ab initio calculations · chiral EFT interactions

1 Introduction

Ab initio nuclear structure theories using 2- (NN) plus 3-nucleon (3N) Hamiltonians derived from chiral effective field theory (EFT) (see [1] for a recent review) connect to the underlying physics of the strong interaction and provide a unique opportunity to understand the nuclear structure and its evolution from first principles. Although recent calculations of excitation energies with chiral NN+3N interactions in light and medium-mass (mainly closed-shell) nuclei have been successful, their extension to other observables remains a challenge. Therefore, data on electromagnetic properties provide an exciting opportunity to constrain NN+3N Hamiltonians derived from chiral EFT in ab initio calculations ranging from Nuclear Lattice EFT [2] to the No-Core Shell Model (NCSM) [3, 4]. The strong sensitivity to the underlying interaction makes these observables prime candidates for testing next-generation chiral Hamiltonians, e.g., the consistent chiral NN+3N interactions at next-to-next-to-next-to-leading order that are being developed now. At the same time, they are a critical test for new ab initio approaches, e.g., the nuclear lattice EFT and shell model with valence-space interactions from an in-medium similarity renormalization group evolution, which are presently being extended to the description of transition observables.

^ae-mail: marina.petri@york.ac.uk

Large-scale NCSM calculations, starting from realistic Hamiltonians without adjustable parameters or effective charges, have been performed for low-lying states of even-even carbon isotopes with $A = 10 - 20$ [5] in order to understand their structural evolution with increasing neutron number. Overall, a strong sensitivity of the electromagnetic observables in ^{16}C to the details of the nuclear Hamiltonian has been found. In particular, a strong suppression of the $2_2^+ \rightarrow 0_{g.s.}^+$ transition has been predicted when the 3N interaction is included. The sensitivity to the presence of the 3N interaction is remarkable. The $2_2^+ \rightarrow 0_{g.s.}^+$ transition strength is suppressed by a factor of ≈ 7 in the calculation with the chiral 3N compared to chiral NN only. At the same time the CD-Bonn potential, a well-tested NN interaction constructed within meson exchange theory and very successful in the description of p -shell spectroscopy, predicts a transition strength larger by a factor of ≈ 20 than the chiral NN+3N interaction. An experimental study of ^{16}C [6] points to the inclusion of 3N forces in order to reproduce the experimental branching ratios of the $2_2^+ \rightarrow 2_1^+$ and $2_2^+ \rightarrow 0_{g.s.}^+$ transitions that have been constrained to $>91.2\%$ and $<8.8\%$, respectively.

The lifetimes of the higher-lying states in ^{16}C are key observables to understand the role of 3N forces and to benchmark ab initio calculations employing interactions developed within chiral effective field theory; see Figure 1 for the current experimental information on the low-lying levels of ^{16}C . A recent experimental investigation of the lifetime of the 2_2^+ state [7] was inconclusive, delivering only a lower limit for the lifetime with a strong dependency on the energy of the γ -ray transition. In this work, we present an improved measurement of the lifetime of the 2_2^+ state and a lower limit for the lifetime of the 4_1^+ state in ^{16}C . We combine our results with previous results on the lifetime of the 2_1^+ state [6, 8] and we compare those with new ab initio calculations. Our work provides a rather complete set of key observables to benchmark present and future ab initio calculations. Indeed, new NCSM calculations using state-of-the-art chiral NN+3N interactions at next-to-next-to-next-to-leading order for both the NN and the 3N contributions reproduce the experimental findings remarkably well.

2 Experimental Details, Analysis and Results

To measure lifetimes of higher-lying excited states in ^{16}C , a Doppler-Shift Attenuation Method (DSAM) experiment was employed at the Tandem Linac Accelerator System (ATLAS) of the Argonne National Laboratory (ANL). A 40 MeV ^9Be beam bombarded a 1.38 mg/cm² ^9Be target. To realise the Doppler-Shift

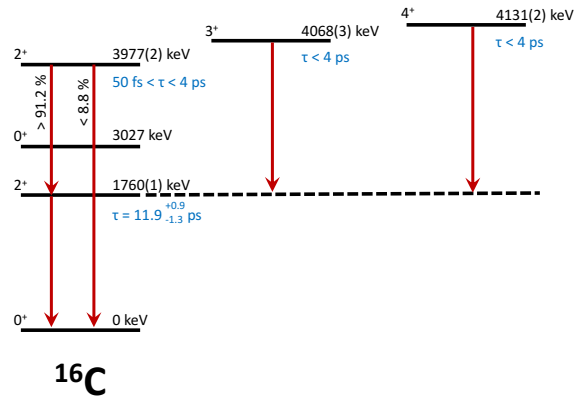


Fig. 1 Spectroscopic information on the bound excited states of ^{16}C ; lifetime information are extracted from Refs. [6–9].

Attenuation measurement, a 38.4 mg/cm² Au degrader was evaporated on the back of the ^9Be target. Excited states in ^{16}C were accessed through the fusion-evaporation channel $^9\text{Be}(^9\text{Be}, 2\text{p})^{16}\text{C}$, as demonstrated in [8]. The emitted γ rays were measured using the Gammasphere array [10], consisting of 87 Compton suppressed HPGe detectors positioned at 16 different polar angles, θ , with respect to the beam axis. To select events that correspond to ^{16}C (i.e., the two-proton (2p) exit channel of the fusion-evaporation reaction), the Microball charged-particle detector [11] was placed inside the scattering chamber and operated in coincidence with Gammasphere.

A two-dimensional (2D) plot of the laboratory energy of the emitted γ rays (i.e., not Doppler corrected) versus the Gammasphere detector angle θ in coincidence with two protons detected in Microball are shown in Figure 2. The 2_1^+ and 4_1^+ decays of ^{16}C are clearly seen as vertical lines, which indicates that the decay occurs after the nucleus has stopped in the Au degrader (decaying thus with zero velocity ($\beta = v/c = 0$) and not presenting any Doppler shift). This puts a lower limit for the lifetime of the 4_1^+ state, discussed in Section 2.2. The $3_1^+ \rightarrow 2_1^+$ transition of ^{16}C overlaps with the $7/2_1^+ \rightarrow 5/2_1^+$ state of ^{15}N (the relatively strong 1p2n exit channel); the latter channel produces random background in Microball which could not be removed in the present analysis and which hinders any conclusion on the lifetime of the 3_1^+ state. The ^{22}Ne lines originate from $(^9\text{Be}, 2\text{pn})$ reactions induced by oxygen layers on the surface of the target. This contamination in the γ -ray spectrum has been used to validate the analysis procedure with the help of the known lifetime of the 4^+ state of ^{22}Ne , see Figure 3; more details can be found in [12]. This also demonstrates the sensitivity of our setup to lifetimes of the order of few hundred

femtoseconds. The 2_2^+ state of ^{16}C cannot be seen in the 2p gated spectrum because it is weakly populated in the fusion-evaporation reaction and the γ -ray energy spectrum is dominated by background. More detailed investigations have thus been performed, as described in the Section 2.1.

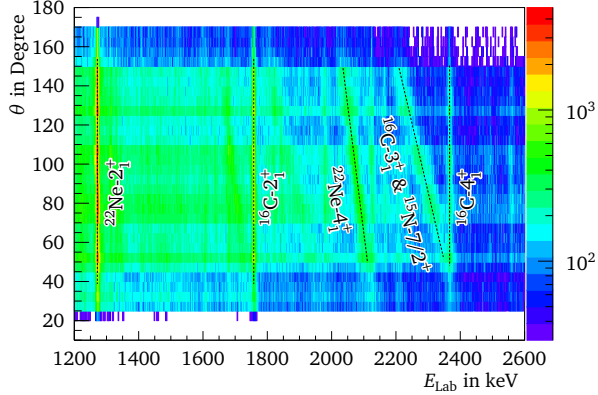


Fig. 2 (Colour online) Radiation-detection angle θ versus laboratory energy E_{Lab} for 2p Microball-gated γ -ray events for the target/degrader setting. Dominant γ rays from other fusion-evaporation reactions, as well as those from the reaction channel of interest are indicated with a dotted line, the corresponding isotope and the initial state of the γ -ray transition is given. Other transitions visible but not marked on the plot correspond to the ^{23}Ne $7/2^+ \rightarrow 5/2^+$ 1701 keV transition and to the ^{15}N $5/2_2^+ \rightarrow 5/2_1^+$ 1884 keV transition.

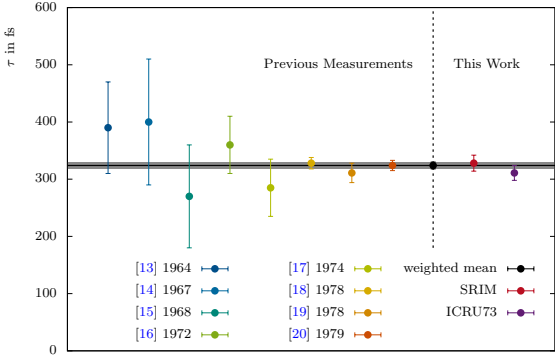


Fig. 3 (Colour online) Temporal development of the measured lifetimes for the 4_1^+ state in ^{22}Ne . The eight values from the previous measurements are taken from [13–20] respectively. They lead to the uncertainty weighted mean of $324(6)$ fs [21], which is shown as a black point and as a grey uncertainty band. The results from this work, illustrated by the red (SRIM stopping powers) and purple (ICRU73 stopping powers) data points, are in excellent agreement with the previous measurements.

2.1 Lifetime of the 2_2^+ State

In order to access the 2_2^+ state, we need to look at an even more selective channel, i.e., the 2p gated γ rays in coincidence with the $2_1^+ \rightarrow 0_{g.s.}^+$ γ -ray transition of ^{16}C . Figure 4 shows the γ -ray spectra in coincidence with the $2_1^+ \rightarrow 0_{g.s.}^+$ transition for Gammasphere angles from 69.82° to 162.73° . For smaller angles no transitions of ^{16}C could be observed with certainty. The three dashed lines in the spectra mark the expected center-of-mass energy for the three transitions $4_1^+ \rightarrow 2_1^+$, $3_1^+ \rightarrow 2_1^+$ and $2_2^+ \rightarrow 2_1^+$, which all feed the 2_1^+ state (see Figure 1). In Figure 4 one clearly sees the $4_1^+ \rightarrow 2_1^+$ transition as a stopped peak for most angles. The $2_2^+ \rightarrow 2_1^+$ transition could be observed as a moving peak for six angles. The red fit-functions at the $2_2^+ \rightarrow 2_1^+$ transition peaks in Figure 4 are defined by a single Gaussian function using the binned-likelihood method recommended in case of low statistics; same results are obtained using the center of gravity approach. The results for the mean value of these fits are plotted against $\cos(\theta)$ in Figure 5, where θ is the central angle of the Gammasphere detectors¹. The fit, described by

$$E_{\text{Lab}}(\bar{\beta}, \theta) = E_{\text{cm}} \frac{\sqrt{1 - \bar{\beta}^2}}{1 - \bar{\beta} \cos \theta}, \quad (1)$$

yields $E_{\text{cm}} = 2213(4)$ keV, in agreement with the uncertainty weighted mean value of $2217(2)$ keV from [6, 8], and $\bar{\beta}_{\text{Exp}} = 0.03905(245)$ for the mean decay velocity.

In order to draw any conclusion on the lifetime of the state using the mean velocity of the decay ($\bar{\beta}_{\text{Exp}}$), we need to know the initial velocity of the excited ^{16}C ions. Although one could calculate this velocity from the fusion-evaporation reaction dynamics, this does not take into account the experimental conditions, e.g., detection angles, proton detection efficiency, etc. We therefore determined this initial velocity experimentally. To achieve this, a similar measurement albeit using a very thin (0.093 mg/cm 2), self-supporting ^9Be target was performed. By fitting the laboratory γ -ray energy as a function of $\cos(\theta)$ of the strongly populated $2_1^+ \rightarrow 0_{g.s.}^+$ transition (as similarly done in Figure 5), we extract the mean velocity of the decay. The energy loss in such thin target is negligible and therefore the velocity of the particle during the decay is approximately the same as the velocity the particle has directly after

¹We performed Monte Carlo simulations to find the average angle (as opposed to the central angle) θ . The difference is very small and the results remain robust; the maximum difference between the central angle and average angle is 0.4 degrees, and the maximum difference of the cosine of the central angle, the cosine of the average angle, and the average of cosine angle is of the order 10^{-3} .

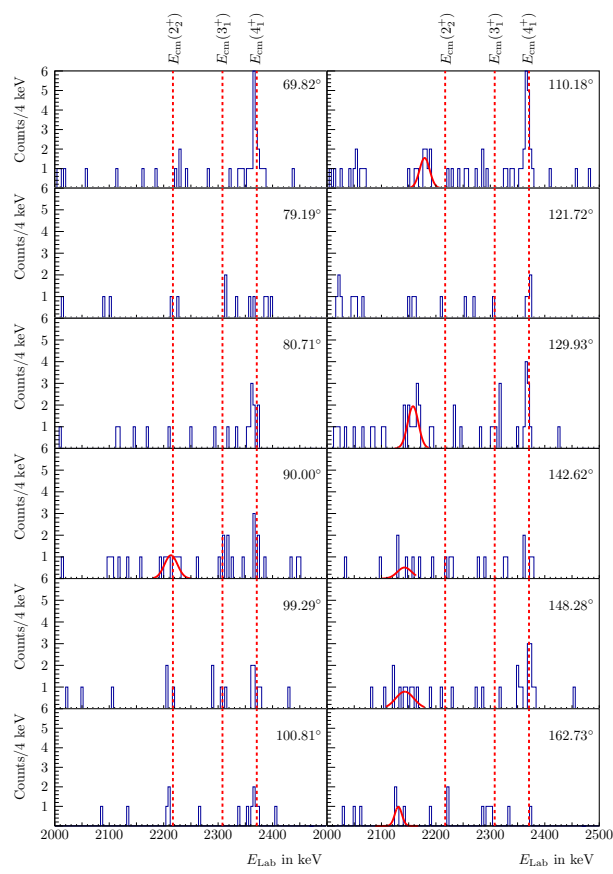


Fig. 4 (Colour online) Gamma-ray spectra in coincidence with the $2_1^+ \rightarrow 0_{g.s.}^+$ transition for Gammasphere angles from 69.82° to 162.73° and a 2p coincidence in Microball. The spectra for the discrete Gammasphere angles are obtained for a 2σ γ gate on the $2_1^+ \rightarrow 0_{g.s.}^+$ transition with $E_{cm} = 1760$ keV and $\sigma = 3.2$ keV. The red dashed lines mark the expected center-of-mass energies for the $4_1^+ \rightarrow 2_1^+$ ($E_{cm}(4_1^+)$), $3_1^+ \rightarrow 2_1^+$ ($E_{cm}(3_1^+)$) and $2_2^+ \rightarrow 2_1^+$ ($E_{cm}(2_2^+)$) transitions [6, 8]. The red fit-functions are defined by a single Gaussian function using the binned-likelihood method recommended in case of low statistics.

its creation. The latter was determined to be $\bar{\beta}_{TO} = 0.04527(44)$ (TO stands for target-only runs, i.e., no degrader). This method has the advantage that all systematics of the experimental setup are already included in the extracted mean velocity $\bar{\beta}$, such as systematic effects of proton losses in the target, the response of the Microball and Gammasphere detectors, and the fusion-evaporation kinematics. The response of Microball is particularly important as it is strongly angle dependent due to, e.g., different absorbers used at each Microball angle.

To extract the lifetime of the state from the determined velocities at the time of creation² and the decay

² $\bar{\beta}_{TO} = 0.04527(44)$

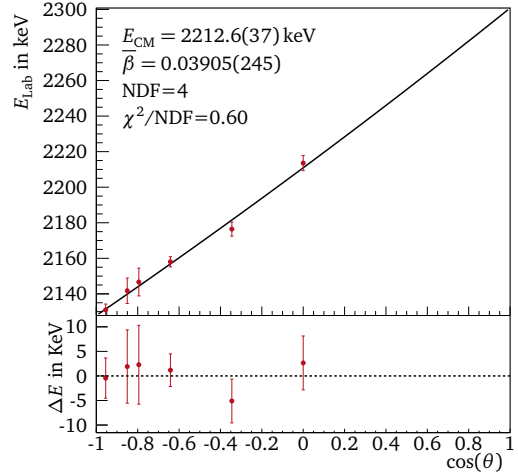


Fig. 5 E_{Lab} versus $\cos(\theta)$ fit for the $2_2^+ \rightarrow 2_1^+$ transition of ^{16}C . The E_{Lab} values are extracted from the Gaussian fits shown in Figure 4. The black fit-function is described by Equation 1. The lower plot shows the residuals ΔE of the fit which is shown in the upper part.

velocity³, we employ Geant4 to simulate the slowing-down process and study the decay of the state of interest through the same target/degrader material budget as in the experiment for various lifetimes. Indeed, we simulated excited ^{16}C ions using their initial velocity $\bar{\beta}_{TO}$ and taking into account the thickness of the target (1.38 mg/cm^2), how the latter affects the fusion-evaporation cross section and how the $\bar{\beta}_{TO}$ would turn into a distribution of initial velocities according to where the ^{16}C ions were created along the target thickness.

An important parameter in our simulations that will affect the lifetime of the state is the stopping powers that are employed by Geant4. The standard database used by Geant4 for energy loss of ions in matter is the ICRU73 dataset, which includes a mixture of calculated and measured stopping powers for ions heavier than helium [22]. Geant4 is developed and optimized for high-energy experiments. Following the investigations of [23], two changes in the simulation process are applied to get a more accurate slowing down behaviour of ions at low energies. First, the ICRU73 stopping powers are replaced by stopping powers which are calculated with the program SRIM, a software-package which reproduces well the stopping behaviour of ions for different materials over a wide energy range [24]. Secondly, the so-called *forced stepping* method is added to the simulation code, where the simulation evaluates the behaviour of the particle no later than a given distance set by the user. The *forced stepping* distance should be set to small values for low-energy physics, as is done in this work.

³ $\bar{\beta}_{Exp} = 0.03905(245)$

The simulation was performed for various lifetimes of the 2_2^+ state and the results were analyzed much in the same way as was done with the experimental data, i.e., the mean-decay velocity was extracted by plotting the laboratory energy versus the $\cos(\theta)$ as in Figure 5. The resulting mean decay velocities from the simulations, $\bar{\beta}_{\text{Sim}}$, as a function of simulated lifetimes are shown in Figure 6. The intersection between the simulated results and the experimentally defined velocity $\bar{\beta}_{\text{Exp}}$, and in particular the upper limit of the uncertainty band, defines the lower limit of the lifetime. This results in $\tau \gtrsim 244$ fs for SRIM stopping powers for the 2_2^+ state.

To constrain the lifetime of the 2_2^+ state further, an additional evaluation method is applied to the data. The number of counts in the moving-peak component (C_{Moving}) are compared to the number of counts in the stopped-peak component (C_{Stopped}). The longer the lifetime of the state, the more decays take place at rest and therefore the stopped-peak component increases. For the evaluation of the 2_2^+ state, Geant4 simulations are performed for different lifetimes and the ratio

$$R_{\text{Sim}}(\tau_{\text{Sim}}) = \frac{C_{\text{Stopped}}(\tau_{\text{Sim}})}{C_{\text{Moving}}(\tau_{\text{Sim}})} \quad (2)$$

is calculated for different lifetimes and for each Gammasphere angle separately. Then the following function is fitted to the simulated data, as shown in Figure 7(a),

$$R_{\text{Sim}}(\tau_{\text{Sim}}) = a \cdot \tau_{\text{Sim}}^2 + b \cdot \tau_{\text{Sim}}. \quad (3)$$

The number of counts in the moving-peak component in the experimental data ($C_{\text{Moving,Exp}}$) is used to deduce how many counts should appear in the simulated stopped-peak component ($C_{\text{Stopped,Sim}}$) for a given lifetime:

$$C_{\text{Stopped,Sim}}(\tau_{\text{Sim}}) = C_{\text{Moving,Exp}} \cdot R_{\text{Sim}}(\tau_{\text{Sim}}). \quad (4)$$

The result for 110.18° is shown as a black function in Figure 7(b). The blue band around the function shows its uncertainty, i.e., the uncertainty from $C_{\text{Moving,Exp}}$ as well as the fit uncertainties. By comparing the experimental number of counts $C_{\text{Stopped,Exp}}$ for the stopped-peak component with $C_{\text{Stopped,Sim}}(\tau_{\text{Sim}})$, we get an upper limit for the lifetime of the 2_2^+ state. The horizontal (orange) line with yellow band in Figure 7(b) shows the experimental result for the stopped-peak component of $C_{\text{Stopped,Exp}}=1(1)$ counts. Here, the mean value from $C_{\text{Stopped,Exp}}$, including its uncertainty $u(C_{\text{Stopped,Exp}})$, can be seen as an upper limit for the number of counts in the stopped-peak component, which is still compatible with the experimental data. Hence, all lifetimes for

which the blue and yellow area are overlapping are compatible with the experimental data. Due to this, an upper lifetime limit is obtained by determining the intersection between $C_{\text{Stopped,Sim}}(\tau_{\text{Sim}}) + u[C_{\text{Stopped,Sim}}(\tau_{\text{Sim}})]$ (right end of the blue uncertainty band) and $C_{\text{Stopped,Exp}} + u[C_{\text{Stopped,Exp}}]$ (upper border of the yellow uncertainty band).

For this analysis only the spectra for 110.18° and 129.93° Gammasphere angles are used to reduce statistical uncertainties; these are the only spectra for which we have significant number of counts in the moving-peak component. In addition, in these angles the moving- and stopped-peak component do not overlap, reducing further experimental uncertainties. The analysis is done separately for the 110.18° and 129.93° data and the results are combined by calculating the corresponding mean value. The analysis was also repeated for the extreme target thicknesses to include the target thickness uncertainties in the results. The lifetimes are always longer for the thickest possible target (+10% thickness). Hence, these results are used as a systematic uncertainty for the upper lifetime limit. The latter is γ -ray energy dependent and results to an upper lifetime limit of 376 fs for a center-of-mass transition energy between 2209.0 keV and 2213.5 keV and 446 fs for a center-of-mass transition energy between 2213.5 keV and 2217.0 keV; $E_{\text{cm}} = 2213(4)$ keV as extracted in Figure 5. We have assumed no background in the γ -ray spectrum and the upper lifetime limit is determined at 70% confidence level (C.L.); the C.L. is expected to change, becoming higher or lower, if random background is present in the energy region of the stopped and/or moving component, respectively, see, e.g., [25].

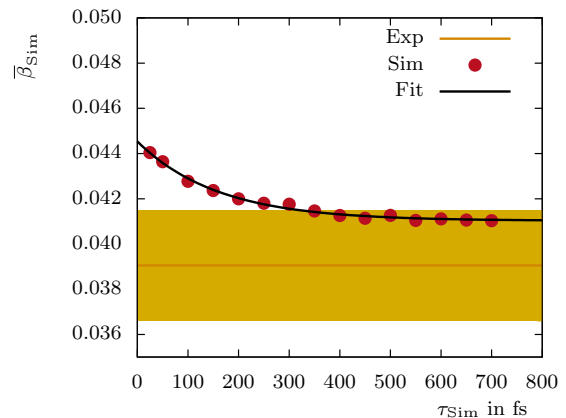


Fig. 6 (Colour online) Simulated mean decay beta $\bar{\beta}_{\text{Sim}}$ versus simulated lifetime τ_{Sim} for the $2_2^+ \rightarrow 2_1^+$ transition of ^{16}C . The initial beta in the simulation was obtained with $\bar{\beta}_{\text{TO}}=0.04527(44)$. The yellow band illustrates the experimental mean decay beta value of $\bar{\beta}_{\text{Exp}}=0.03905(245)$ including its uncertainty.

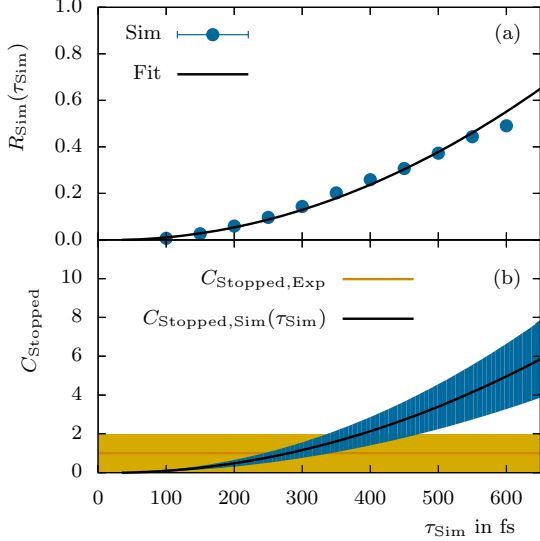


Fig. 7 (a) Ratio of counts between the moving and stopped peak component for the $2_2^+ \rightarrow 2_1^+$ transition of ^{16}C for 110.18° and results from the Geant4 simulations with Equation 3 as a fit-function. (b) This fit-function scaled with $C_{\text{Moving},\text{Exp}}$, which represents $C_{\text{Stopped},\text{Sim}}(\tau_{\text{Sim}})$. The blue band around the function shows its uncertainty including the uncertainty from $C_{\text{Moving},\text{Exp}}$ as well as the fit uncertainties. Also $C_{\text{Stopped},\text{Exp}}=1(1)$ counts is plotted in orange for which the uncertainty is shown as a yellow band.

Figure 8 summarizes the results for the lifetime of the 2_2^+ of ^{16}C . Using SRIM stopping powers and taking the systematic uncertainties into account, the lifetime can be expected in a range from 244 fs to 376 fs for a center-of-mass transition energy between 2209.0 keV and 2213.5 KeV and the lifetime can be expected in a range from 244 fs to 446 fs for a center-of-mass transition energy between 2213.5 keV and 2217.0 keV. In Figure 8 results from Ciemala et al. [7] are also shown. The figure shows the upper lifetime limit (black dashed horizontal line) and the most likely lifetime range (blue boxes) using the estimated lower lifetime from the mean decay beta method. The results from Ciemala et al. are marked by the red data points. According to Ciemala et al. the transition energy should be located between 2214 keV and 2218 keV and the lifetime depends strongly on this energy as can be seen in Figure 8. Comparing both results, this work suggests a transition energy which is slightly lower than the energy measured by Ciemala et al. In terms of lifetimes, the data points from 2214 keV and 2215 keV are in agreement with the most likely lifetime range from this work. The other data points from Ciemala et al. are lower than the most likely lifetime range from this work.

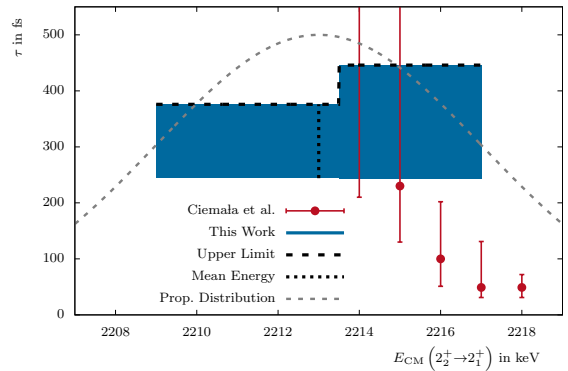


Fig. 8 Results for the lifetime range of the 2_2^+ state in ^{16}C using the count ratio method and SRIM stopping powers. The values from this work are shown as black dashed lines and blue boxes. The horizontal black dashed lines mark the upper lifetime limit while the vertical black dashed line marks the mean γ -ray energy for the $2_2^+ \rightarrow 2_1^+$ transition as measured in this work. The blue boxes mark the most likely lifetime range. The external values shown as red dots are the most recent measurements from Ciemala et al. [7]. The grey dashed function shows the relative probability distribution as a function of the transition energy for our results. It follows a Gaussian distribution with a mean of 2213 keV and a sigma of 4 keV.

2.2 Lifetime of the 4_1^+ State

Figure 2 shows that the $4_1^+ \rightarrow 2_1^+$ transition presents a significant stopped peak, corresponding to a longer lifetime (in the picosecond range) than this method is sensitive to. Therefore, we can only put a lower limit to the lifetime of the 4_1^+ state. Additionally, from Ref. [8] it is already known that the lifetime of the 4_1^+ state should be faster than 4 ps. We can then constrain theoretical calculations by using the range of lifetimes as extracted from this experiment and previous works.

To achieve a proper lower lifetime limit, the experimental γ -ray spectra for each Gammasphere angle are compared to Geant4 simulations. As we discussed in the previous section, the ratio between the stopped and moving component of a γ ray depends strongly on the lifetime of the decaying state. To infer the lower limit of the lifetime of the 4_1^+ state, we look at the ratio of these two peaks in our experiment (in coincidence with two protons detected in Microball) and we compare this with our simulations.

First we investigate whether we have a moving peak in our experimental spectrum. For this purpose a peak on top of the background has to have a maximum height which is larger than the 2σ uncertainty of the background. Everything else is considered as background fluctuations. The 2σ uncertainty of the background will be labelled as M_{BG} hereafter. Additionally, the maximum height of the stopped peak M_{Stopped} from the

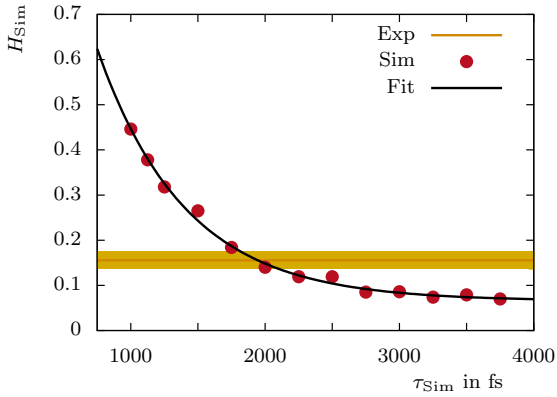


Fig. 9 (Colour online) Estimation of a lower lifetime limit for the 4_1^+ state of ^{16}C using the 148.28° Gammasphere spectrum. Geant4 simulation results for $H_{\text{Sim}}(\tau_{\text{Sim}})$ have been performed using SRIM stopping powers and $\bar{\beta}_{\text{TO}}=0.04527(44)$. The black fit-function is described by Equation 7. The yellow band illustrates the experimental ratio of $H_{\text{Exp}}=0.156(19)$ including its uncertainty.

$4_1^+ \rightarrow 2_1^+$ transition is extracted to calculate the ratio

$$H_{\text{Exp}} = \frac{M_{\text{BG}}}{M_{\text{Stopped}}}. \quad (5)$$

This is performed for those Gammasphere angles for which the $4_1^+ \rightarrow 2_1^+$ transition is resolved clearly in the spectrum, i.e., 121.72° , 129.93° , 142.62° , 148.28° , and 162.73° . For smaller angles the $4_1^+ \rightarrow 2_1^+$ transition interferes with the $7/2_1^+ \rightarrow 5/2_1^+$ transition of ^{15}N and cannot be used in the analysis.

The $4_1^+ \rightarrow 2_1^+$ transition is simulated for different lifetimes of the 4_1^+ state and the ratio

$$H_{\text{Sim}}(\tau_{\text{Sim}}) = \frac{M_{\text{Moving}}}{M_{\text{Stopped}}} \quad (6)$$

is calculated for each simulated lifetime τ_{Sim} , where M_{Moving} is the peak maximum of the moving peak component and M_{Stopped} is the peak maximum of the stopped peak component. A function of the form

$$H_{\text{Sim}}(\tau_{\text{Sim}}) = a \cdot e^{-b\tau_{\text{Sim}}} + c. \quad (7)$$

is then fitted to the simulated data.

In Figure 9 this is shown for the 148.28° Gammasphere angle. To obtain a lower lifetime limit, τ_{Min} , we use the intersection of the fit-function with the experimental ratio H_{Exp} . In the figure this is visualized by the intersection of the black fit-function and the orange line which represents the experimental ratio H_{Exp} . The yellow band around the line represents its statistical uncertainty.

The final result was extracted as the uncertainty weighted mean from all five Gammasphere angles, see

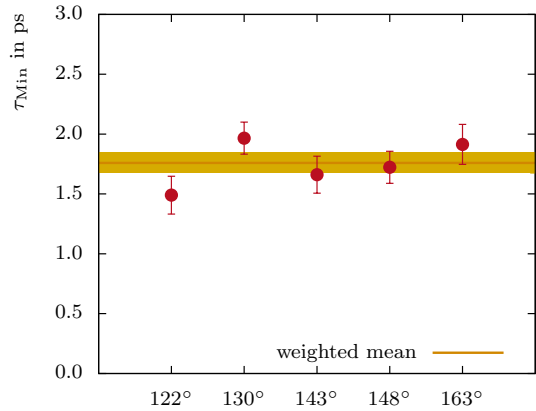


Fig. 10 (Colour online) Results for a lower lifetime limit τ_{Min} for the 4_1^+ state of ^{16}C . The Geant4 simulations were performed for $\bar{\beta}_{\text{TO}}=0.04527(44)$. The yellow band illustrates the uncertainty weighted mean including its 1σ uncertainty for these data points. The uncertainty weighted mean is deduced to $1.95(9)$ ps for SRIM stopping powers.

Figure 10, to be $1.95(9)$ ps and this yields a lower lifetime limit of $\tau_{\text{Min}}=1.9$ ps by subtracting the mean value by its 1σ uncertainty. Additionally, systematic uncertainties due to the target thickness⁴ yield the final result of $\tau_{\text{Min}}=1.9^{+0.0}_{-0.1}(\text{syst}_{\text{target}})$ ps as a lower lifetime limit for the 4_1^+ state of ^{16}C .

Combining the present results with the upper lifetime limit from Ref. [8], the lifetime of the 4_1^+ state is between 1.8 ps and 4 ps which corresponds to a decay rate of $\lambda_{\text{Min}}(4_1^+) = 2.50 \cdot 10^{11} \frac{1}{\text{s}}$ and $\lambda_{\text{Max}}(4_1^+) = 5.55 \cdot 10^{11} \frac{1}{\text{s}}$. Using the experimental transition energy of 2369 keV, the $E2$ transition strength of the $4_1^+ \rightarrow 2_1^+$ state is

$$2.74 \text{ e}^2 \text{ fm}^4 \leq B(E2; 4_1^+ \rightarrow 2_1^+) \leq 6.10 \text{ e}^2 \text{ fm}^4. \quad (8)$$

3 Theory

Electromagnetic transitions in ^{16}C are a particular challenge for ab initio nuclear structure theory. On the one hand, this nucleus is at the upper end of the mass range where conventional ab initio methods, such as the NCSM, can be applied. Moreover, $E2$ observables exhibit a notoriously slow convergence, so that precise converged calculations, e.g., for $B(E2)$ strengths, are beyond our computational capabilities. On the other hand, recent ab initio approaches for medium-mass nuclei, such as the in-medium similarity renormalization group (IM-SRG) and its open-shell extensions, e.g., the valence-space IM-SRG [26, 27] and the in-medium NCSM

⁴The same analysis was performed using a 10% thinner target which would yield a shorter lifetime.

[28], overcome the convergence limitations for ground-state and excitation energies but exhibit deficiencies in the description of $E2$ observables. For the valence-space IM-SRG it was shown that $B(E2)$ transition strengths are severely underestimated in present calculation due to missing three- and multi-body terms in the IM-SRG evolution of the $E2$ operator [29]. In the in-medium NCSM, which uses multi-reference IM-SRG evolved operators for a subsequent NCSM calculation in small model spaces, the situation is more subtle. For some transitions, e.g., the 2_1^+ to ground-state transition in ^{12}C , the in-medium NCSM provides precise results, but for the corresponding transition in ^{16}C the $B(E2)$ is drastically underestimated. Work is under way to fix these limitations by, e.g., extension of the IM-SRG to three-body operators or by tailoring the reference space in the in-medium NCSM to capture all of the relevant collective correlations.

In this work we limit ourselves to direct NCSM calculations for ^{16}C . In order to improve the convergence, particularly of long-range observables like the $E2$, we use a generalized natural-orbital basis instead of the conventional harmonic-oscillator single-particle basis. The natural orbitals as introduced in Ref. [30] have proven extremely useful in connection with the NCSM and other many-body methods—they optimize the model-space convergence and remove the dependence on the oscillator frequency or oscillator length. While this is advantageous for NCSM calculations of energies, a parameter that controls the length scale of the basis is advantageous to assess the convergence systematics in cases where full convergence cannot be reached. Therefore, we use a scaled version of the natural-orbital (SNAT) basis in this work. Starting with a natural orbital basis constructed for a nominal oscillator length of $a_{\text{HO}} = 1.4 \text{ fm}$ we scale all single-particle wave functions to a different length parameter a_{SNAT} , the ratio $a_{\text{SNAT}}/a_{\text{HO}}$ defines the scaling factor by which the wavefunctions are stretched radially. We perform NCSM calculations for a set of length parameters a_{SNAT} and analyze the convergence pattern of the full set.

For all calculations we use state-of-the-art chiral NN+3N interactions at next-to-next-to-next-to-leading order (N³LO) for both the NN and the 3N contributions. This interaction has been introduced in Ref. [31] and provides an excellent description of ground-state energies and charge radii up into the medium-mass regime. We use a free-space SRG transformation of the Hamiltonian and all other operators with $\alpha = 0.08 \text{ fm}^4$ [32, 33]. Since we are dealing with non-converged NCSM calculations, the many-body uncertainties are dominant for the observables discussed here. Therefore, we do not explicitly include the uncertainty estimated for the chi-

ral truncation and we also omit chiral two-body corrections to the $E2$ operator.

In Figure 11 we present the convergence patterns for various $B(E2)$ transition strengths in ^{16}C involving the 0^+ ground state, the first two 2^+ excited states, and the first 4^+ excited state. The colored symbols represent different length parameters a_{SNAT} of the SNAT basis as indicated on the right-hand end of the individual N_{max} sequences. In cases where the HO basis calculations show a different overall trend, we also show N_{max} sequences for four different HO frequencies, as denoted on the left-hand side of the data sequences, for comparison.

The N_{max} sequences for the different transitions show the notorious problem with $E2$ observables in NCSM and other ab initio calculations: they exhibit an extremely slow convergence. None of the calculations shown can be considered fully converged. Moreover, extrapolations to the infinite Hilbert space are difficult and strongly model dependent. Therefore, we take a pragmatic approach and assess the overall convergence pattern and try to estimate the $B(E2)$ for the SNAT basis for an optimal a_{SNAT} length parameter. In two cases, the $2_2^+ \rightarrow 0_{g.s.}^+$ and the $2_1^+ \rightarrow 2_1^+$ transitions, we can identify an optimal value for a_{SNAT} that leads to a constant result for the $B(E2)$ in the two largest model spaces. The maximum difference to the neighboring two a_{SNAT} for the largest N_{max} is used as an uncertainty estimate. These estimates are indicated in panels (b) and (c) of Figure 11 by black horizontal lines with a grey band indicating the uncertainty, the numerical values are summarized in Table 1. This selection is supported by the general trend of the other sequences, which all move towards the estimated value. For the other two cases, the $2_1^+ \rightarrow 0_{g.s.}^+$ and the $4_1^+ \rightarrow 2_1^+$ transition, the calculations for all a_{SNAT} and $\hbar\Omega$ show a monotonic increase with N_{max} . Therefore, within the range of basis parameters used here, we cannot estimate the $B(E2)$ as for the other cases, we can only specify a lower bound given by the maximum value of the $B(E2)$ obtained in the calculations, which is again indicated by a black line in panels (a) and (d) of Figure 11.

4 Discussion

We will now discuss how our experimental findings compare with the new ab initio calculations described in Section 3. In Table 1 we summarize the experimental values for the energy of the $2_1^+, 2_2^+, 4_1^+$ states in ^{16}C , their lifetimes, the branching ratio of the γ -ray decay of the 2_2^+ state from [6], the transition strengths that are implied from the lifetimes of the states, and how they compare with theoretical calculations.

For the $2_1^+ \rightarrow 0_{g.s.}^+$ and $4_1^+ \rightarrow 2_1^+$ transitions, the lifetime can be translated into a $B(E2)$ transition strength directly. However, the 2_2^+ state can decay via the $2_2^+ \rightarrow 0_{g.s.}^+$ and the $2_2^+ \rightarrow 2_1^+$ transition. For the $2_2^+ \rightarrow 0_{g.s.}^+$ transition only an $E2$ component is possible. For the $2_2^+ \rightarrow 2_1^+$, both $M1$ and $E2$ decay modes can dominate. Therefore, the lifetime of the 2_2^+ state, $\tau(2_2^+) = [244, 446]$ fs, can be translated into the total decay rate and compared with theory. The total decay rate of the 2_2^+ state, $\lambda_{\text{Total}}(2_2^+)$, is

$$\lambda_{\text{Total}}(2_2^+) = \lambda(E2; 2_2^+ \rightarrow 0_{g.s.}^+) + \lambda(E2; 2_2^+ \rightarrow 2_1^+) + \lambda(M1; 2_2^+ \rightarrow 2_1^+) = 1/\tau(2_2^+) \quad (9)$$

with

$$2.25 \cdot 10^{12} \text{ s}^{-1} \leq \lambda_{\text{Total}}(2_2^+) \leq 4.10 \cdot 10^{12} \text{ s}^{-1}. \quad (10)$$

From [6] it is also known that the branching ratio for the $2_2^+ \rightarrow 0_{g.s.}^+$ transition is limited to

$$\text{BR}(2_2^+ \rightarrow 0_{g.s.}^+) = \frac{\lambda(E2; 2_2^+ \rightarrow 0_{g.s.}^+)}{\lambda_{\text{Total}}(2_2^+)} < 8.8\%. \quad (11)$$

From Eqs. (10) and (11) we obtain an upper limit for the $E2$ strength of the $2_2^+ \rightarrow 0_{g.s.}^+$ transition of

$$B(E2; 2_2^+ \rightarrow 0_{g.s.}^+) < 0.30 \text{ e}^2 \text{fm}^4. \quad (12)$$

The total decay rate (Eq. (9)) of the 2_2^+ state can be expanded as

$$\begin{aligned} \lambda_{\text{Total}}(2_2^+) &= \\ &= \frac{1.22 \cdot 10^9}{\text{s}} \left(\frac{E_\gamma(2_2^+ \rightarrow 0_{g.s.}^+)}{\text{MeV}} \right)^5 \frac{B(E2; 2_2^+ \rightarrow 0_1^+)}{\text{e}^2 \text{fm}^4} \\ &+ \frac{1.22 \cdot 10^9}{\text{s}} \left(\frac{E_\gamma(2_2^+ \rightarrow 2_1^+)}{\text{MeV}} \right)^5 \frac{B(E2; 2_2^+ \rightarrow 2_1^+)}{\text{e}^2 \text{fm}^4} \\ &+ \frac{1.76 \cdot 10^{13}}{\text{s}} \left(\frac{E_\gamma(2_2^+ \rightarrow 2_1^+)}{\text{MeV}} \right)^3 \frac{B(M1; 2_2^+ \rightarrow 2_1^+)}{\mu_N^2}. \end{aligned} \quad (13)$$

By combining this with the experimentally known transition energies and the constraints from Eqs. (10) and (12), one can deduce an explicit constraint on the three transition strengths.

We can now confront the NCSM calculation with this experimental information. The ab initio results obtained with the new generation of chiral NN+3N interactions are compatible with the experimental data for all observables for the first time. Previous NCSM calculations reported in Ref. [5], which are based on the CD Bonn 2000 phenomenological NN interaction without an initial 3N force, fail to reproduce the experimental pattern of $B(E2)$ values. As illustrated in

Table 1, the $B(E2)$ value for the $2_1^+ \rightarrow 0_{g.s.}^+$ transition is underestimated and the $B(E2)$ for the $2_2^+ \rightarrow 0_{g.s.}^+$ transition is overestimated significantly. This leads to an underestimation of the lifetime of the 2_2^+ state and the branching ratio for the $2_2^+ \rightarrow 2_1^+$ transition by a factor of 3.

The chiral NN+3N interaction at N³LO used in the present NCSM calculations predicts a large value for the $2_1^+ \rightarrow 0_{g.s.}^+$ transition and a small value for the $2_2^+ \rightarrow 0_{g.s.}^+$ transition in good agreement with experiment. The resulting total transition rate obtained from Eq. (13) and, thus, the lifetime of the 2_2^+ state are in excellent agreement with experiment when using the experimental transition energies. Stated differently, the transition strengths obtained in the calculation fulfill the constraints provided by the experimental data via Eq. (13). Using the calculated transition energies from the NCSM we still find a good agreement of the 2_2^+ lifetime with experiment. It is important to note that the calculated excitation energies agree with experiment within uncertainties, however, the lifetime is very sensitive to transition energies and thus amplifies their theory uncertainties. The branching ratio for the $2_2^+ \rightarrow 2_1^+$ transition is also in good agreement with experiment irrespective of the choice of energies. In addition, the lower bounds derived from the NCSM sequences for the $B(E2)$ of the $2_1^+ \rightarrow 0_{g.s.}^+$ and the $4_1^+ \rightarrow 2_1^+$ transition are compatible with the experimental data, thus providing a consistent description of the complete spectroscopy of these states.

The calculations presented in Ref. [5] also included results for a first generation of chiral NN+3N interactions using a local 3N interaction at N2LO. Though these calculations were not converged and only ratios of $B(E2)$ transition strengths were discussed, some important features were observed. Most notably, the suppression of the $B(E2)$ for the $2_2^+ \rightarrow 0_{g.s.}^+$ through the inclusion of the 3N interaction. The same mechanism is at play for the new-generation chiral NN+3N interactions used in this work. However, the first-generation NN+3N interaction produces significantly smaller absolute values, e.g., for the $B(E2)$ for the $2_1^+ \rightarrow 0_{g.s.}^+$ transition. Comparing results at fixed $N_{\text{max}} = 6$, the $B(E2)$ obtained in Ref. [5] is about 50% smaller and, thus, incompatible with experiment. This is in line with the general observation that the first-generation chiral NN+3N interactions produce too small radii starting from the mid p-shell. This deficiency has been fixed in the new-generation of interactions and translates to larger $E2$ strength.

Table 1 Level energies (E), lifetimes (τ), transition strengths ($B(E/M)$), total decay rates (λ_{Total}) and branching ratios (BR) for ^{16}C from this work (unless a reference is provided), and how they compare with theory (see text for details). The theoretical BR, λ_{Total} and τ are calculated using both experimental and theoretical transition energies, indicated with ^a and ^b, respectively.

State		Experiment	NCSM NN+NNN	NCSM CDB2k [5]	Unit
2_1^+	$E(2_1^+)$ $B(E2; 2_1^+ \rightarrow 0_{g.s.}^+)$	1759.0 ± 0.4 $4.1_{-0.3}^{+0.5}$ [6, 8, 34]	1650 ± 100 > 4.39	2430 ± 50 2.2 ± 0.9	keV $e^2 \text{fm}^4$
2_2^+	$E(2_2^+)$	3972 ± 4	4200 ± 250	4900 ± 300	keV
	$B(E2; 2_2^+ \rightarrow 2_1^+)$	Eqs. (10), (13)	5.27 ± 0.95	4.4 ± 1.8	$e^2 \text{fm}^4$
	$B(M1; 2_2^+ \rightarrow 2_1^+)$	Eqs. (10), (13)	0.012 ± 0.003	0.013 ± 0.001	μ_N^2
	$B(E2; 2_2^+ \rightarrow 0_{g.s.}^+)$	< 0.30 [6]	0.44 ± 0.27	4.84 ± 1.98	$e^2 \text{fm}^4$
	$\text{BR}(2_2^+ \rightarrow 2_1^+)$	> 91.2 [6]	83 ± 11^a 86 ± 11^b	32 ± 9^a 19 ± 10^b	%
	$\lambda_{\text{Total}}(2_2^+)$ $\tau(2_2^+)$	[2.25, 4.10] [244, 446]	3.2 ± 0.7^a 316 ± 66^a	4.9 ± 1.5^b 204 ± 64^b	20.6 ± 8.6^b 116 ± 32^a 49 ± 20^b
4_1^+	$E(4_1^+)$ $B(E2; 4_1^+ \rightarrow 2_1^+)$ $\tau(4_1^+)$	4129.0 ± 0.2 [2.74, 6.10] [1.8, 4]	4500 ± 250 > 2.6 $< 4.22^a$	6170 ± 100 1.96 ± 0.80 $5.59_{-1.62}^{+3.86} a$ $0.57_{-0.16}^{+0.40} b$	keV $e^2 \text{fm}^4$ ps

^a using the experimental transition energy

^b using the theoretical transition energy

5 Summary

Meaningful limits to the lifetimes of higher-lying excited states in ^{16}C were extracted in order to benchmark ab initio calculations. Indeed, the structure of ^{16}C has been highlighted as an important touchstone for these calculations, showing strong sensitivity to the underlying nuclear interaction, and in particular to the inclusion of 3N forces. Our experiment has delivered key experimental data to constrain modern nuclear theories. Ab initio NCSM calculations employing new interactions derived within chiral EFT show remarkable agreement with experiment, a very promising step towards describing nuclear structure from first principles. They also show that $E2$ transitions present a specific challenge for ab initio methods and require further methodological improvements to provide more accurate predictions for these important observables.

Acknowledgements This work was supported by the Deutsche Forschungsgemeinschaft (DFG, German Research Foundation) – Projekt-Nr. 279384907 – SFB 1245, the Royal Society under contract number UF150476, the UK STFC under grant numbers ST/L005727/1 and ST/P003885/1, the U.S. Department of Energy, Office of Science, Office of Nuclear Physics, under Contract Nos. DE-AC02-06CH11357 (ANL), DE-AC02-05CH11231 (LBNL) and DE-AC05-00OR22725 (ORNL), the U.S. NSF under grant No. PHY-2012522 and the National Research Foundation of South Africa (Grant No. 118846). This research used resources of ANL’s ATLAS Facility, which

is a DOE Office of Science User Facility. The authors thank J. T. Anderson and M. B. Oberling for technical support, J. P. Greene for the preparation of the target, and the ATLAS accelerator crew for their supreme effort.

References

1. E. Epelbaum, H.W. Hammer, U.G. Meißner, *Reviews of Modern Physics* **81**(4), 1773 (2009). DOI 10.1103/revmodphys.81.1773
2. E. Epelbaum, H. Krebs, D. Lee, U.G. Meißner, *Phys. Rev. Lett.* **106**, 192501 (2011). DOI 10.1103/PhysRevLett.106.192501. URL <https://link.aps.org/doi/10.1103/PhysRevLett.106.192501>
3. P. Navrátil, J.P. Vary, B.R. Barrett, *Phys. Rev. Lett.* **84**, 5728 (2000). DOI 10.1103/PhysRevLett.84.5728. URL <https://link.aps.org/doi/10.1103/PhysRevLett.84.5728>
4. P. Navrátil, S. Quaglioni, I. Stetcu, B.R. Barrett, *Nucl. Phys. A* **36**(8), 083101 (2009). DOI 10.1088/0954-3899/36/8/083101. URL <https://doi.org/10.1088/0954-3899/36/8/083101>
5. C. Forssén, R. Roth, P. Navrátil, *J. Phys. G Nucl. Part. Phys.* **40**(5), 055105 (2013). DOI 10.1088/0954-3899/40/5/055105
6. M. Petri, S. Paschalis, R.M. Clark, P. Fallon, A.O. Macchiavelli, K. Starosta, T. Baugher, D. Bazin, L. Cartegni, H.L. Crawford, M. Cromaz,

U. Datta Pramanik, G. de Angelis, A. Dewald, A. Gade, G.F. Grinyer, S. Gros, M. Hackstein, H.B. Jeppesen, I.Y. Lee, S. McDaniel, D. Miller, M.M. Rajabali, A. Ratkiewicz, W. Rother, P. Voss, K.A. Walsh, D. Weisshaar, M. Wiedeking, B.A. Brown, C. Forssén, P. Navrátil, R. Roth, Phys. Rev. C **86**, 044329 (2012). DOI 10.1103/PhysRevC.86.044329. URL <https://link.aps.org/doi/10.1103/PhysRevC.86.044329>

7. M. Ciemała, S. Ziliani, F.C.L. Crespi, S. Leoni, B. Fornal, A. Maj, P. Bednarczyk, G. Benzoni, A. Bracco, C. Boiano, S. Bottoni, S. Brambilla, M. Bast, M. Beckers, T. Braunroth, F. Camera, N. Cieplińska-Oryńczak, E. Clément, S. Coelli, O. Dorvaux, S. Erturk, G. de France, C. Fransen, A. Goldkuhle, J. Grebosz, M.N. Harakeh, L.W. Iskra, B. Jacquot, A. Karpov, M. Kicińska Habior, Y. Kim, M. Kmiecik, A. Lemasson, S.M. Lenzi, M. Lewitowicz, H. Li, I. Matea, K. Mazurek, C. Michelagnoli, M. Matejska-Minda, B. Million, C. Müller-Gattermann, V. Nanal, P. Napiorkowski, D.R. Napoli, R. Palit, M. Rejmund, C. Schmitt, M. Stanoiu, I. Stefan, E. Vardaci, B. Wasilewska, O. Wieland, M. Zieblinski, M. Zielińska, A. Ataç, D. Barrientos, B. Birkenbach, A.J. Boston, B. Cederwall, L. Charles, J. Collado, D.M. Cullen, P. Désesquelles, C. Domingo-Pardo, J. Dudouet, J. Eberth, V. González, J. Goupil, L.J. Harkness-Brennan, H. Hess, D.S. Judson, A. Jungclaus, W. Korten, M. Labiche, A. Lefevre, R. Menegazzo, D. Mengoni, J. Nyberg, R.M. Perez-Vidal, Z. Podolyak, A. Pullia, F. Recchia, P. Reiter, F. Saillant, M.D. Salsac, E. Sanchis, O. Stezowski, C. Theisen, J.J. Valiente-Dobón, J.D. Holt, J. Menéndez, A. Schwenk, J. Simonis, Phys. Rev. C **101**, 021303 (2020). DOI 10.1103/PhysRevC.101.021303

8. M. Wiedeking, P. Fallon, A.O. Macchiavelli, J. Gibelin, M.S. Basunia, R.M. Clark, M. Cromaz, M.A. Deleplanque, S. Gros, H.B. Jeppesen, P.T. Lake, I.Y. Lee, L.G. Moretto, J. Pavan, L. Phair, E. Rodriguez-Vietiez, L.A. Bernstein, D.L. Bleuel, J.T. Burke, S.R. Lesher, B.F. Lyles, N.D. Scielzo, Phys. Rev. Lett. **100**, 152501 (2008). DOI 10.1103/PhysRevLett.100.152501. URL <https://link.aps.org/doi/10.1103/PhysRevLett.100.152501>

9. H.J. Ong, N. Imai, D. Suzuki, H. Iwasaki, H. Sakurai, T.K. Onishi, M.K. Suzuki, S. Ota, S. Takeuchi, T. Nakao, Y. Togano, Y. Kondo, N. Aoi, H. Baba, S. Bishop, Y. Ichikawa, M. Ishihara, T. Kubo, K. Kurita, T. Motobayashi, T. Nakamura, T. Okumura, Y. Yanagisawa, Phys. Rev. C **78**, 014308 (2008). DOI 10.1103/PhysRevC.78.014308. URL <https://link.aps.org/doi/10.1103/PhysRevC.78.014308>

10. I.Y. Lee, Nucl. Phys. A **520**, c641 (1990). DOI 10.1016/0375-9474(90)91181-P

11. D. Sarantites, P.F. Hua, M. Devlin, L. Sobotka, J. Elson, J. Hood, D. LaFosse, J. Sarantites, M. Maier, Nucl. Instr. Meth. Phys. Res. A **381**(2), 418 (1996). DOI 10.1016/S0168-9002(96)00785-1. URL <http://www.sciencedirect.com/science/article/pii/S0168900296007851>

12. M. Mathy, Electromagnetic Properties of Light Neutron-Rich Nuclei - Lifetime Measurements of ^{16}C and ^{23}Ne . Ph.D. thesis, Technische Universität Darmstadt (2020)

13. M.A. Eswaran, C. Broude, Can. J. Phys. **42**, 1311 (1964)

14. E.K. Warburton, J.W. Olness, A.R. Poletti, Phys. Rev. **160**, 938 (1967). DOI 10.1103/PhysRev.160.938. URL <https://link.aps.org/doi/10.1103/PhysRev.160.938>

15. W. Kutschera, D. Pelte, G. Schrieder, Nucl. Phys. A **111**(3), 529 (1968). DOI 10.1016/0375-9474(68)90237-6

16. C. Broude, P. Engelstein, M. Popp, P. Tandon, Phys. Lett. B **39**(2), 185 (1972). DOI 10.1016/0370-2693(72)90769-1. URL <http://www.sciencedirect.com/science/article/pii/0370269372907691>

17. L.K. Fifield, R.W. Zurmühle, D.P. Balamuth, Phys. Rev. C **10**, 1785 (1974). DOI 10.1103/PhysRevC.10.1785. URL <https://link.aps.org/doi/10.1103/PhysRevC.10.1785>

18. L. Ekström, D. Scherpenzeel, G. Engelbertink, H. Aarts, H. Eggenhuisen, Nucl. Phys. A **295**(3), 525 (1978). DOI 10.1016/0375-9474(78)90190-2. URL <http://www.sciencedirect.com/science/article/pii/0375947478901902>

19. L.K. Fifield, J. Asher, A.R. Poletti, J. Phys. G Nucl. Part. Phys. **4**(3), L65 (1978). DOI 10.1088/0305-4616/4/3/005. URL <https://doi.org/10.1088%2F0305-4616%2F4%2F3%2F005>

20. J. Forster, T. Alexander, G. Ball, W. Davies, I. Mitchell, K. Winterbon, Nucl. Phys. A **313**(3), 397 (1979). DOI 10.1016/0375-9474(79)90509-8. URL <http://www.sciencedirect.com/science/article/pii/0375947479905098>

21. M. Shamsuzzoha Basunia. Nucl. Data Sheets **127**, 69(2015). <https://www.nndc.bnl.gov/nudat2/getdataset.jsp?nucleus=22NE&unc=nds> (2015). [Online; accessed 31th July 2020]

22. ICRU, Journal of the International Commission on Radiation Units and Measurements **5**(1), iii (2005). DOI 10.1093/jicru/ndi002. URL <https://doi.org/10.1093/jicru/ndi002>

//doi.org/10.1093/jicru/ndi002

23. S. Heil, Simulation of gamma-ray detector arrays for nuclear physics experiments. Master's thesis, Technische Universität Darmstadt (2015)
24. J.F. Ziegler, M. Ziegler, J. Biersack, Nucl. Instr. Meth. Phys. Res. B **268**(11), 1818 (2010). DOI 10.1016/j.nimb.2010.02.091. URL <http://www.sciencedirect.com/science/article/pii/S0168583X10001862>. 19th International Conference on Ion Beam Analysis
25. G.J. Feldman, R.D. Cousins, Phys. Rev. D **57**, 3873 (1998). DOI 10.1103/PhysRevD.57.3873. URL <https://link.aps.org/doi/10.1103/PhysRevD.57.3873>
26. K. Tsukiyama, S.K. Bogner, A. Schwenk, Phys. Rev. C **85**, 061304 (2012). DOI 10.1103/PhysRevC.85.061304
27. S.R. Stroberg, A. Calci, H. Hergert, J.D. Holt, S.K. Bogner, R. Roth, A. Schwenk, Phys. Rev. Lett. **118**(3), 032502 (2017). DOI 10.1103/PhysRevLett.118.032502
28. E. Gebrerufael, K. Vobig, H. Hergert, R. Roth, Phys. Rev. Lett. **118**(15), 152503 (2017). DOI 10.1103/PhysRevLett.118.152503
29. S.R. Stroberg, J. Henderson, G. Hackman, P. Ruotsalainen, G. Hagen, J.D. Holt, Phys. Rev. C **105**(3), 034333 (2022). DOI 10.1103/PhysRevC.105.034333
30. A. Tichai, J. Müller, K. Vobig, R. Roth, Phys. Rev. C **99**(3), 034321 (2019). DOI 10.1103/PhysRevC.99.034321
31. T. Hüther, K. Vobig, K. Hebeler, R. Machleidt, R. Roth, Phys. Lett. B **808**, 135651 (2020). DOI 10.1016/j.physletb.2020.135651
32. R. Roth, J. Langhammer, A. Calci, S. Binder, P. Navratil, Phys. Rev. Lett. **107**, 072501 (2011). DOI 10.1103/PhysRevLett.107.072501
33. R. Roth, A. Calci, J. Langhammer, S. Binder, Phys. Rev. C **90**(2), 024325 (2014). DOI 10.1103/PhysRevC.90.024325
34. H.J. Ong, N. Imai, D. Suzuki, H. Iwasaki, H. Sakurai, T.K. Onishi, M.K. Suzuki, S. Ota, S. Takeuchi, T. Nakao, Y. Togano, Y. Kondo, N. Aoi, H. Baba, S. Bishop, Y. Ichikawa, M. Ishihara, T. Kubo, K. Kurita, T. Motobayashi, T. Nakamura, T. Okumura, Y. Yanagisawa, Phys. Rev. C **78**, 014308 (2008). DOI 10.1103/PhysRevC.78.014308. URL <https://link.aps.org/doi/10.1103/PhysRevC.78.014308>

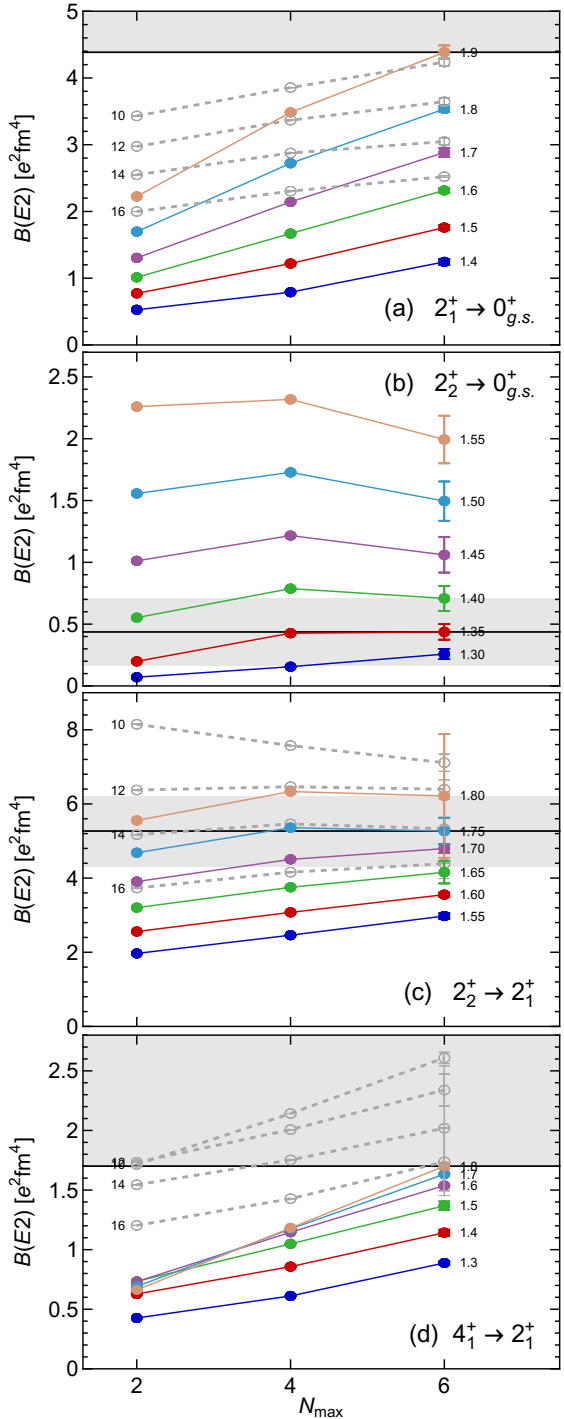


Fig. 11 Results of ab initio NCSM calculations for the $B(E2)$ transition strengths involving the 0^+ ground state, the first two 2^+ excited states, and the first 4^+ excited state. The colored symbols show the N_{\max} dependence obtained with the SNAT basis for different values of a_{SNAT} [fm] as indicated on the right-hand-side of each sequence. The grey symbols show N_{\max} sequences obtained with the HO basis for different values of $\hbar\Omega$ [MeV] as indicated on the left-hand-side of each sequence.